



# A Nanomechanical Study on Deciphering the Stickiness of SARS-CoV-2 on Inanimate Surfaces

Lei Xie,<sup>†</sup> Fenglin Liu,<sup>†</sup> Jifang Liu,<sup>\*</sup> and Hongbo Zeng<sup>\*</sup>

Cite This: *ACS Appl. Mater. Interfaces* 2020, 12, 58360–58368

Read Online

ACCESS |

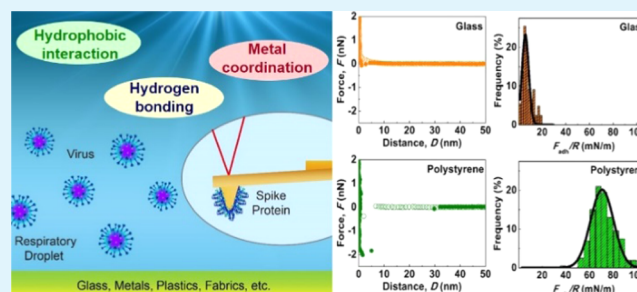
Metrics & More

Article Recommendations

Supporting Information

**ABSTRACT:** The SARS-CoV-2 virus that causes the COVID-19 epidemic can be transmitted via respiratory droplet-contaminated surfaces or fomites, which urgently requires a fundamental understanding of intermolecular interactions of the coronavirus with various surfaces. The corona-like component of the outer surface of the SARS-CoV-2 virion, named spike protein, is a key target for the adsorption and persistence of SARS-CoV-2 on various surfaces. However, a lack of knowledge in intermolecular interactions between spike protein and different substrate surfaces has resulted in ineffective preventive measures and inaccurate information. Herein, we quantified the surface interaction and adhesion energy of SARS-CoV-2 spike protein with a series of inanimate surfaces via atomic force microscopy under a simulated respiratory droplet environment. Among four target surfaces, polystyrene was found to exhibit the strongest adhesion, followed by stainless steel (SS), gold, and glass. The environmental factors (e.g., pH and temperature) played a role in mediating the spike protein binding. According to systematic quantification on a series of inanimate surfaces, the adhesion energy of spike protein was found to be (i) 0–1 mJ/m<sup>2</sup> for hydrophilic inorganics (e.g., silica and glass) due to the lack of hydrogen bonding, (ii) 2–9 mJ/m<sup>2</sup> for metals (e.g., alumina, SS, and copper) due to the variation of their binding capacity, and (iii) 6–11 mJ/m<sup>2</sup> for hydrophobic polymers (e.g., medical masks, safety glass, and nitrile gloves) due to stronger hydrophobic interactions. The quantitative analysis of the nanomechanics of spike proteins will enable a protein–surface model database for SARS-CoV-2 to help generate effective preventive strategies to tackle the epidemic.

**KEYWORDS:** spike protein, intermolecular interaction, surface adhesion, COVID-19, surface forces



## 1. INTRODUCTION

Since December 2019, the COVID-19 outbreak caused by SARS-CoV-2 has led to over 70 million of confirmed cases and over 1.6 million deaths in 218 countries.<sup>1–5</sup> The main transmission routes of SARS-CoV-2 indicate that this respiratory disease can spread by inhalation and/or direct contact with droplets of infected people as well as indirect contact with contaminated surfaces that carry respiratory droplets from infected persons.<sup>1–5</sup> While social distancing is proved to be an effective approach to inhibit the human–human transmission through direct routes, infections through indirect contact remain challenging to combat, owing to the invisible spreading paths and unclear surface behaviors of the new coronavirus.<sup>5–8</sup> Therefore, identifying the surface interactions of SARS-CoV-2 has become essential for prohibiting virus transmission via surface contaminations. The Munster group evaluated the persistence of SARS-CoV-2 by accessing virus decay rates in aerosols and on several typical substrates,<sup>9</sup> and similar studies were also conducted on other respiratory viruses such as SARS,<sup>9,10</sup> MERS,<sup>11,12</sup> and Ebola,<sup>13</sup> as shown in Table 1. Despite the significant progress achieved, it remains unclear in terms of the intermolecular

interactions involved, such as adsorption and binding strengths of the virus on typical substrates, which are critical for evaluating viral loads on those target surfaces. Thus, detailed studies toward the nanomechanics of the virus-contaminated surfaces are urgently needed to determine the interaction mechanisms at the nanoscale, as well as their influences on viral persistence.

Spike protein refers to a class I fusion protein that is located at the surface of a coronavirus virion (illustrated in Figure 1A).<sup>14–16</sup> Consisting of more than 1000 amino acids, the spike protein can assemble into crownlike nanoarchitecture that allows the viral binding and fusion to host cell membranes through molecular recognition.<sup>17–19</sup> With regard to the structure of the new coronavirus, there are two main subunits in the spike protein named S1 and S2, the former of which is

**Received:** September 17, 2020

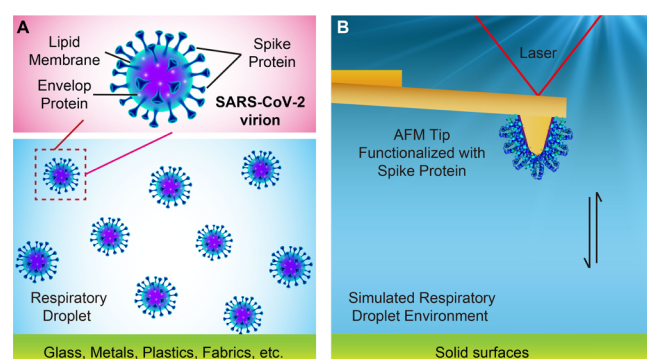
**Accepted:** December 7, 2020

**Published:** December 18, 2020



**Table 1. Persistence of Selected Coronaviruses on Typical Inanimate Surfaces**

virus type	inanimate surfaces	environment	persistence	references
SARS-CoV-2	copper	21–23 °C; 40% humidity	4 h	9
	cardboard	21–23 °C; 40% humidity	24 h	9
	SS	21–23 °C; 40% humidity	48 h	9
	plastic	21–23 °C; 40% humidity	72 h	9
MERS-CoV	SS	20 °C	48 h	11,12
	plastic	20 °C	48 h	11,12
Ebola-CoV	SS	21–27 °C; 40–80% humidity	11–27 h	13
	plastic	21–27 °C; 40–80% humidity	11–43 h	13
	Tyvek	21–27 °C; 40–80% humidity	15–52 h	13
SARS-CoV	copper	21–23 °C; 40% humidity	8 h	9
	cardboard	21–23 °C; 40% humidity	8 h	9
	SS	21–23 °C; 40% humidity	48 h	9
	plastic	21–23 °C; 40% humidity	72 h	9
	metal	room temperature	5 days	10
	wood	room temperature	4 days	10
	paper	room temperature	24 h	10
	glass	21 °C	4 days	10

**Figure 1.** (A) Schematic of SARS-CoV-2 virions in respiratory droplets contaminating solid substrates such as glass, metals, plastics, and fabrics (down), and the zoomed-in structure of the SARS-CoV-2 virion (up). (B) Schematic of the experimental setup for measuring the interaction forces between the spike protein-functionalized AFM tip and various solid surfaces in simulated respiratory droplet environments.

responsible for ACE2 receptor binding using its receptor-binding domain, while the latter is managing the subsequent membrane fusion.<sup>16,17,20</sup> Considering the critical role of the spike protein in viral infection, characterizing the adsorption behavior and adhesion strength of spike protein can shed light on the molecular mechanism how the new coronavirus contaminates the surfaces of inanimate substrates. The active subunit S1 has been recognized as a good candidate to understand the adsorption and adhesion of spike protein at the molecular level owing to its representative structure and function.<sup>17–19</sup> Being the powerful nanomechanical techniques, atomic force microscopy (AFM) and surface force apparatus

(SFA) have been widely employed to quantitatively characterize the intermolecular interactions, including adhesion and single-molecule binding, of a variety of biological molecules in vapor or liquid media.<sup>21–32</sup> As compared to SFA that requires molecularly smooth surfaces with at least one surface being transparent, AFM is more versatile to quantify the interaction forces of the materials that cannot be easily accessed by SFA. The unique, flexibility, and accuracy of AFM make it feasible to access the interaction mechanism of spike protein at the nanoscale.

To systematically investigate the adsorption behavior and interaction mechanism of COVID-19 spike protein, herein, a direct and quantitative analysis of surface interactions of spike protein was presented with respect to adsorption, kinetics, and intermolecular forces in the pico/nanonewton range (schematic illustrated in Figure 1B). A series of inanimate surfaces, including glass, plastics, metals, fabrics, and so forth, were applied to systematically evaluate the adsorption behaviors of the spike protein. In particular, we focused on four targeted surfaces (i.e., glass, gold, stainless steel (SS), and polystyrene-(PS)), which represent the most commonly used materials ranging from inorganics and organics to metals and composites/hybrids. We also discussed the key factors affecting the spike protein binding and explored the protein–surface interaction mechanisms under simulated respiratory droplets, as well as proposed feasible strategies to modulate the binding of spike protein with inanimate surfaces. This work will improve the fundamental understanding associated with the adsorption and adhesion mechanisms of spike protein on various solid substrates, thereby providing guidelines for developing preventive/protective equipment and optimizing current public measures against COVID-19 pandemic.

## 2. RESULTS AND DISCUSSION

### 2.1. Adsorption of Spike Protein on Various Surfaces.

Figure 2 shows the AFM topography images of glass, gold, SS, and PS surfaces before and after the adsorption of spike protein. The bare glass, gold, SS, and PS surfaces exhibit a root-mean-square (RMS) roughness of 0.3–0.7 nm, and such smooth surfaces allow the accurate observation of protein adsorption. It is noted that the uniform grainlike pattern on bare metal (i.e., gold and SS) surfaces is arising from their metal particles. After spike protein adsorption, all the surfaces become rough with the obvious binding of spike protein as indicated by the white dots shown in Figure 2. The spike protein adsorbed on glass is sparsely distributed with a considerable size. In contrast, the size of the spike protein adsorbed on gold and SS is relatively small, and the distribution of the adsorbed spike protein is much denser for SS. However on PS, the size of the adsorbed protein becomes even smaller, and an ultra-dense distribution of protein pattern is observed ( $2 \times 2 \mu\text{m}^2$  image shown in Figure S1). The smaller size and denser distribution of the adsorbed spike protein reveal the preferential binding of spike protein with the surface instead of self-aggregation. Therefore, spike protein most preferentially adsorbs on PS followed by SS and gold. On the other hand, the adsorption of spike protein on glass is relatively weaker, as compared to the other three substrates.

**2.2. Quantitative Force Measurements.** To unravel the nanomechanics of spike protein interacting with various solid surfaces, the gold-coated AFM probe (including the AFM tip, cantilever, and cantilever base) is self-assembled with 11-mercaptopundecanoic acid, which subsequently covalently

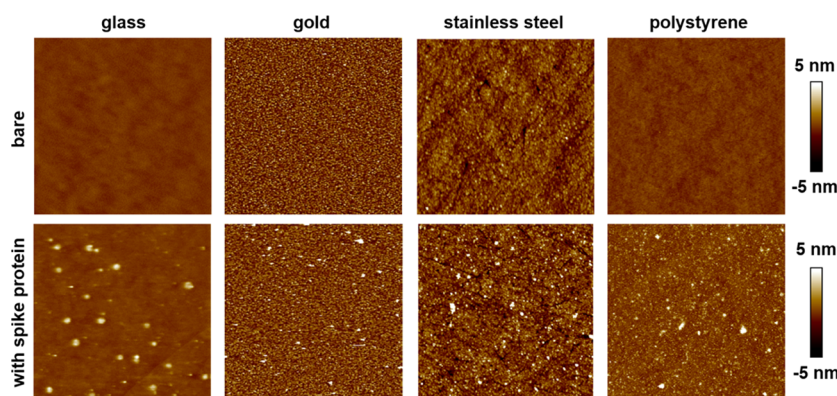


Figure 2. AFM topography images ( $5 \times 5 \mu\text{m}^2$ ) of glass, gold, SS, and PS before and after the adsorption of spike protein.

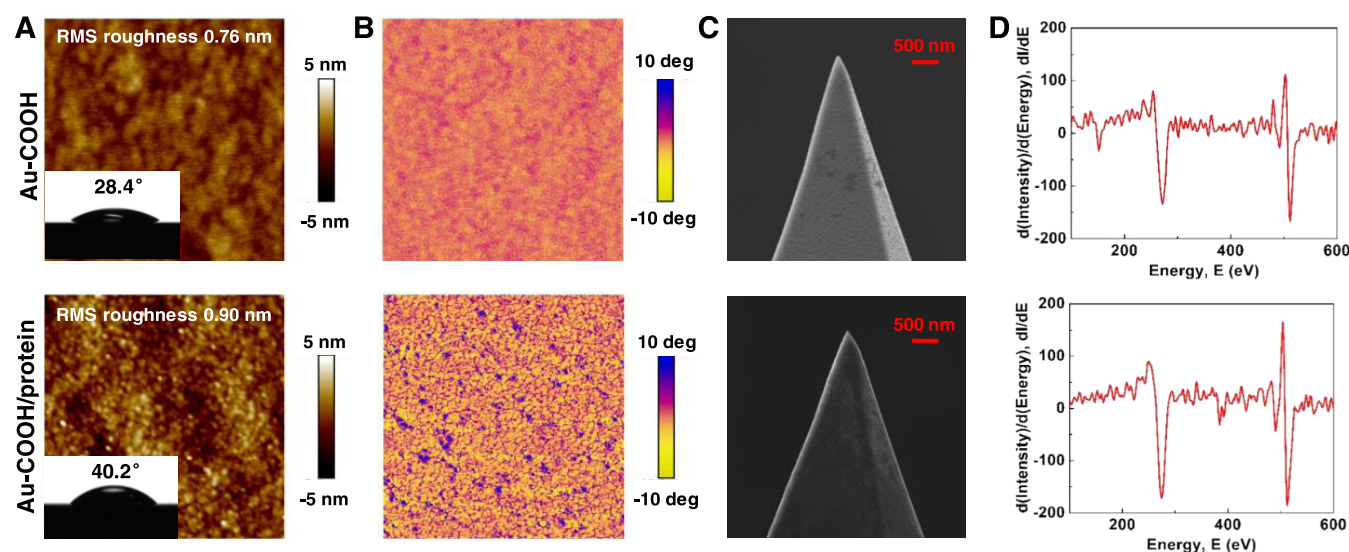


Figure 3. Characterization of the gold-coated AFM probe functionalized with carboxyl groups (up) and spike protein (down): (A) AFM topography image ( $2 \times 2 \mu\text{m}^2$ ) with the water contact angle (inset) on the cantilever base of the AFM probe, (B) phase image ( $2 \times 2 \mu\text{m}^2$ ) of the cantilever base of the AFM probe, (C) HIM on the AFM tip, and (D) Auger electron microscopy on the AFM tip.

bonds with spike protein via the carbodiimide crosslinking strategy.<sup>21,33</sup> The prepared AFM probe was characterized by AFM imaging, contact angle measurements, helium ion microscopy (HIM), and Auger electron spectroscopy (AES). As demonstrated in Figure 3A,B, the AFM probe without and with protein coating displays distinct morphologies and phase images, with spike protein closely and uniformly packing on the AFM probe that enhances RMS roughness from 0.76 to 0.90 nm. Meanwhile, the water contact angle increases from  $28.4^\circ \pm 0.6^\circ$  for the AFM probe without protein modification to  $40.2^\circ \pm 0.8^\circ$  for the protein-functionalized AFM probe (inset of Figure 3A), which suggests that the AFM probe becomes relatively hydrophobic after the protein modification. HIM is a unique surface-sensitive imaging technique that enables the high-resolution imaging of insulating proteins adsorbed at subnanometer resolution.<sup>34</sup> As shown in Figure 3C and Figure S2, the tip of the COOH-functionalized AFM probe displays the grainlike pattern of gold; instead, an evident coverage of nonconductive substances is detected for the tip of the protein-functionalized AFM probe. AFM imaging, water contact angle measurement, and HIM imaging all reveal the successful grafting of spike protein on the AFM probe, which is also further confirmed by the AES analysis where an additional

nitrogen Auger peak at  $\sim 369$  eV appears for the protein-functionalized AFM tip (Figure 3D).

The adsorption and adhesion of the virus outer protein on the surface that occur in droplet environments right after a virus-containing-droplet impacts and attaches to a solid surface are the key to the mechanism how the virus contaminates the surface. The intermolecular forces of spike protein in droplet environments play a central role in the adsorption and adhesion of spike protein on substrate surfaces. To ensure the accuracy of force measurements, force mapping was performed on bare surfaces in an area of  $5 \times 5 \mu\text{m}^2$  using the protein-functionalized AFM probe to acquire a two-dimensional array of force-separation profiles at  $10 \times 10$  points (100 consecutive force-separation measurements). Force mapping was performed in at least three different regions of the substrate surface and at least two independently prepared samples of the same batch. The interaction forces measured between the protein-functionalized AFM tip and selected surfaces that are ubiquitous in daily life, including glass, gold, SS, and PS, during the approach–separation cycle under the typical simulated respiratory droplet condition (10 mM NaCl solution at pH 5.6 and  $23^\circ\text{C}$ ) are shown in Figure 4 (left). For spike protein interacting with glass, the measured force–distance profile (orange open symbols) shows a purely



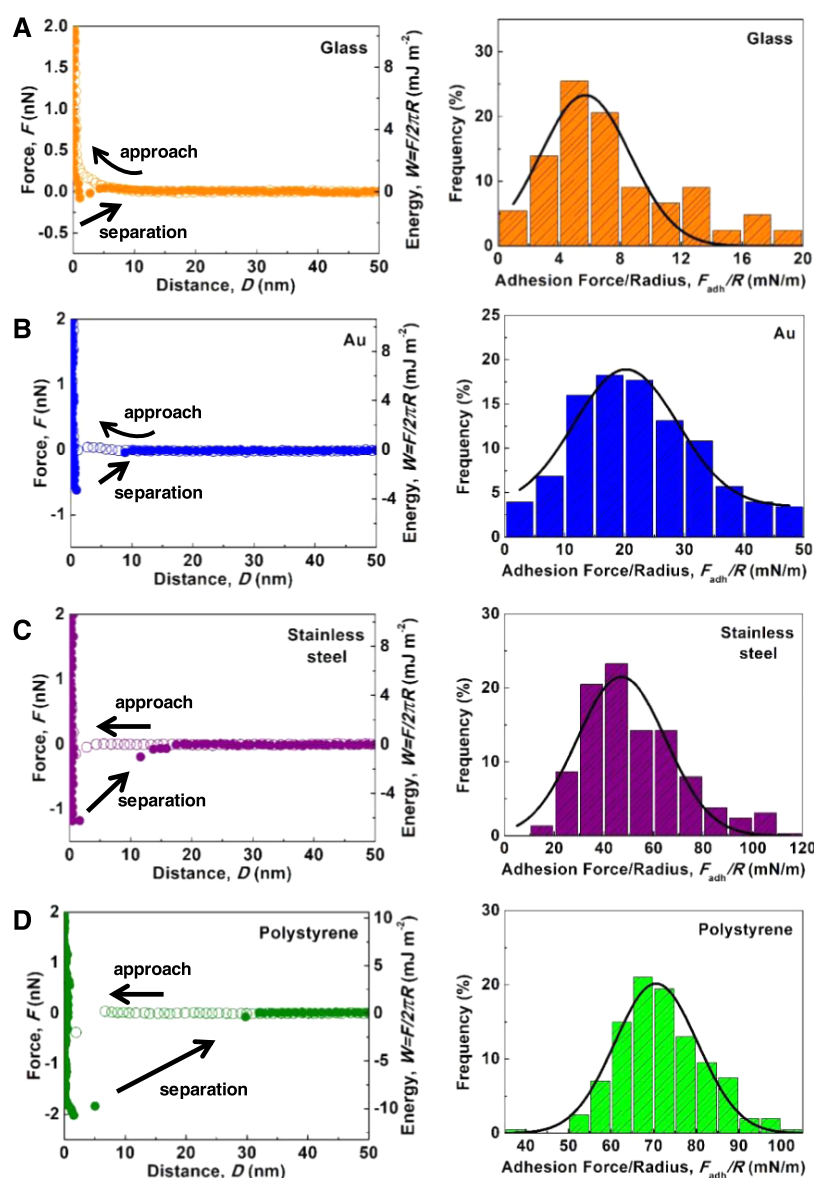


**Figure 4.** Force–distance profiles between the spike protein-functionalized AFM tip and different solid substrates in 10 mM NaCl solution at pH 5.6 and 23 °C (approach data: open symbols and separation data: solid symbols) and the histogram of normalized adhesion force  $F_{adh}/R$  with the fitted Gaussian distribution: (A) glass, (B) gold, (C) SS, and (D) PS.

repulsive force during approach. Zeta potential measurements (Table S1) show that the isoelectric point of spike protein is below pH 5.6, while glass always carries the negative charges under the testing condition;<sup>35</sup> therefore, the measured repulsion is attributed to the repulsive electrical double layer (EDL) force. Upon separation (orange solid symbols), an interfacial adhesion is occasionally detected, probably contributed by the short-range hydrogen bonding between the side chains of amino acids (e.g., lysine, asparagine, and tyrosine) in the spike protein and glass surface. For gold (blue symbols) and SS (purple symbols), in addition to the long-range EDL repulsion, an attractive force starting from a separation distance of 3–4 nm is measured during approach because of the relatively strong van der Waals (VDW) force for metal-involved systems.<sup>36</sup> The adhesion force for gold and SS during separation is mainly induced by the strong coordination interaction between metal atoms and specific sites of spike protein (e.g., carboxyl group and aromatic ring of amino

acids),<sup>37</sup> which is evidently stronger than the adhesion force measured for glass. The spike protein–PS interaction (green symbols) exhibits a strong attraction during approach that induces a “jump-in” phenomenon at ~7 nm. Evidently, the attraction measured is stronger and has a longer range than VDW contribution and considered as the hydrophobic interaction between hydrophobic PS and hydrophobic moieties of spike protein (e.g., hydrophobic side chains of tyrosine). Such strong hydrophobic interaction enables intimate contact between the spike protein and PS, which correspondingly triggers a considerable adhesion during separation.

Based on the adhesion forces measured during separation (300–500 events), the histograms of normalized adhesion force,  $F_{adh}/R$ , are established and fitted by the Gaussian distribution (solid curve) as shown in Figure 4 (right). The magnitude of average normalized adhesion force follows the trend: glass ( $5.71 \pm 0.36$  mN/m) < gold ( $20.23 \pm 0.66$  mN/m)

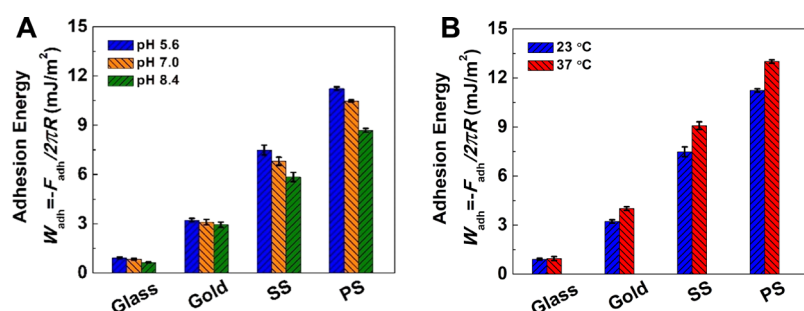


**Figure 5.** Average adhesion energy  $W_{adh} = -F_{adh}/2\pi R$  between the spike protein-functionalized AFM tip and solid surfaces, including glass, gold, SS, and PS, in 10 mM NaCl solution (A) at 23 °C under the effect of pH: 5.6, 7.0, and 8.4 and (B) at pH 5.6 under the effect of temperature: 23 and 37 °C.

m) < SS ( $47.02 \pm 1.89$  mN/m) < PS ( $70.58 \pm 0.63$  mN/m). Based on the Derjaguin–Muller–Toporov model  $W_{adh} = -F_{adh}/2\pi R$  that correlates the normalized adhesion force ( $F_{adh}/R$ ) of a sphere on a plane with the adhesion energy per unit area ( $W_{adh}$ ) of two flat surfaces of the same materials,<sup>36,38–40</sup> the average adhesion energy is obtained as  $\sim 0.91$  mJ/m<sup>2</sup> for glass,  $\sim 3.22$  mJ/m<sup>2</sup> for gold,  $\sim 7.48$  mJ/m<sup>2</sup> for SS, and  $\sim 11.23$  mJ/m<sup>2</sup> for PS, respectively. The adhesion energy between the spike protein and these substrates could be contributed by surface interactions involving hydrogen bonding, hydrophobic interaction, and coordination interaction.

Glass can form hydrogen bonding with the side chains of amino acids in spike protein. Considering the theoretically simulated hydrogen bond energy for protein in solution ( $2.09$ – $6.28$  kJ/mol)<sup>41</sup> and the measured adhesion energy ( $0.91$  mJ/m<sup>2</sup> for protein–glass), there only exists one effective hydrogen bond between spike protein and glass within an area of over  $2.76$  nm  $\times$   $2.76$  nm. The possible reason for such a low bonding efficiency is that the entropic (or steric) effect restricts the optimization of spike protein toward the preferential formation of hydrogen bonds.<sup>42</sup> As compared to the spike protein–glass interaction, the adhesion energy mainly arising from hydrophobic interaction of PS with spike protein is even 10 times stronger, revealing the dominant role of hydrophobic interaction in modulating the adhesion of spike protein (or stickiness of new coronavirus), particularly under the nano-confined regime. The hydrophobic interaction energy is expressed as  $W_{HB} = 2\gamma \exp(-D/D_0)$  for the symmetric cases (e.g., PS–PS interaction in water), where  $\gamma$  is the interfacial energy,  $D_0$  is the decay length of hydrophobic interaction, and  $D$  is the separation distance.<sup>36,43</sup> From the thermodynamic perspective,  $W_{HB} \approx 2\gamma = 79$  mJ/m<sup>2</sup> for PS–PS interaction as  $D$  approaches zero.<sup>36,43</sup> It is noted that the adhesion energy of  $\sim 11.23$  mJ/m<sup>2</sup> for the spike protein–PS interaction is approximately one seventh of the adhesion energy of PS–PS interaction, which indicates that the hydrophobic moiety of spike protein that contributes to the hydrophobic interaction with PS only accounts for a small portion of the entire protein molecule. Metals interacting with spike protein display the adhesion energies that are evidently stronger than those for glass but relatively weaker than those for PS. It is known that metals could form a coordination complex with specific binding sites of protein, and the magnitude of metal–protein binding energy is dependent on the binding capability of the metal and the number of binding sites on the protein. Thus, metals with relatively weaker binding capability (e.g., gold as compared to SS) exhibit smaller adhesion energy, while the relatively weaker adhesion

energies for gold and SS, as compared with that for PS, are likely due to the limited metal–protein binding sites.

### 2.3. Effect of Environmental Factors on Adhesion.

The respiratory droplet normally displays a pH value ranging from 5.6 to 8.4, and the environmental temperature is also varied for different seasons and regions, which could affect the intermolecular interactions of spike protein and thus alter its adsorption behavior and the stickiness of the new coronavirus on substrates. To further unravel the impact of environmental conditions on the interaction mechanism of spike protein, the adhesion energy of spike protein with solid surfaces was measured in 10 mM NaCl solution at different pH values (Figure 5A) and temperatures (Figure 5B). As shown in Figure 5A (with the histogram shown in Figure S3), with pH increasing from 5.6 to 7.0 and 8.4, the adhesion energy slightly drops from  $\sim 0.91$  mJ/m<sup>2</sup> to  $\sim 0.84$  and  $\sim 0.65$  mJ/m<sup>2</sup> for glass as well as from  $\sim 3.22$  mJ/m<sup>2</sup> to  $\sim 3.09$  and  $\sim 2.93$  mJ/m<sup>2</sup> for gold. In contrast, the adhesion energy for the SS and PS cases is more pH-dependent. In particular, the adhesion energy for SS is dramatically reduced from  $\sim 7.48$  mJ/m<sup>2</sup> at pH 5.6 to  $\sim 6.80$  mJ/m<sup>2</sup> at pH 7.0 and  $\sim 5.84$  mJ/m<sup>2</sup> at pH 8.4, while the adhesion energy for PS also significantly decreases from  $\sim 11.23$  mJ/m<sup>2</sup> at pH 5.6 to  $\sim 10.47$  mJ/m<sup>2</sup> at pH 7.0 and  $\sim 8.69$  mJ/m<sup>2</sup> at pH 8.4. Because spike protein, glass, gold, SS, and PS all carry negative charges over the pH range investigated,<sup>35,44,45</sup> it is reasonable that the electrostatic repulsion is strengthened with the increase of pH, which ultimately weakens the adhesion energy and triggers the pH-mediated adhesion.

The role of temperature in altering the adhesion energy is shown in Figure 5B (with the histogram shown in Figure S4). As the temperature increases from 23 to 37 °C, the adhesion energy for glass almost remains unchanged ( $0.91$ – $0.95$  mJ/m<sup>2</sup>), while the adhesion energy dramatically increases from  $\sim 3.22$  to  $\sim 4.01$  mJ/m<sup>2</sup> for gold and from  $\sim 7.48$  to  $\sim 9.08$  mJ/m<sup>2</sup> for SS. It is known that enhanced temperature could improve the binding activity of metal–protein interaction, thereby increasing the adhesion energy. It is known that the entropy-driven hydrophobic interaction is also temperature-dependent.<sup>46</sup> The possible conformational rearrangement in spike protein and PS upon heating results in increased entropy, which is the main reason the adhesion for spike protein–PS interaction increases from  $\sim 11.23$  mJ/m<sup>2</sup> at 23 °C to  $\sim 13.00$  mJ/m<sup>2</sup> at 37 °C. Although the overall trend of average adhesion energy “glass < gold < SS < PS” remains the same regardless of pH and temperature, the environmental factors to a certain degree could contribute to the alternation of protein adhesion, suggesting that the new coronavirus is more readily

to stick to solid materials in an acidic environment and at a high temperature.

**2.4. Adhesion of Spike Protein with Different Materials.** In addition to glass, gold, SS, and PS, we also select a variety of other inorganic, metallic, and polymeric materials for probing their intermolecular forces with spike protein in droplet environments. Figure 6 summarizes the

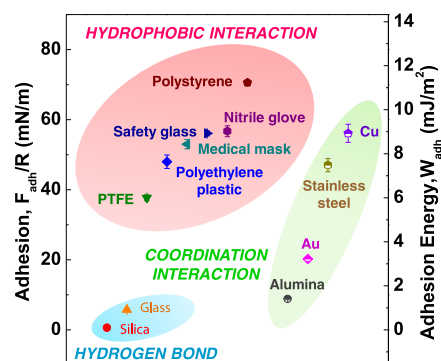


**Figure 6.** Normalized adhesion force  $F_{adh}/R$  and average adhesion energy  $W_{adh} = -F_{adh}/2\pi R$  between the spike protein-functionalized AFM tip and a variety of solid materials in 10 mM NaCl solution at pH 5.6 and 23 °C.

normalized adhesion force and average adhesion energy between the spike protein-functionalized AFM tip and a variety of solid materials in 10 mM NaCl solution at pH 5.6 and 23 °C (with the histogram shown in Figure S5). The hydrophilic inorganic surfaces, such as glass and silica, exhibit the lowest adhesion energy (0–1 mJ/m<sup>2</sup>), revealing the negligible role of hydrogen bonding in the adhesion of spike protein. On the other hand, hydrophobic polymeric materials, including PS, polyethylene plastic, and even low-surface-energy polytetrafluoroethylene (PTFE), can achieve very high adhesion energy (6–11 mJ/m<sup>2</sup>), which indicates the significance of hydrophobic interaction in the adhesion of spike protein. Because the proteins binding to the substrate surfaces rely on their hydrophilicity, the adhesion results demonstrate that the spike protein preferentially binds to hydrophobic surfaces as compared to hydrophilic cases. It is noted that the interaction mechanism between the spike protein and hydrophobic surfaces in aqueous solution is different from that in air. The adsorption of particles or droplets onto hydrophobic commercial masks in air could be mainly due to electrostatic attraction, while the major contribution of the interaction mechanism between the spike protein and hydrophobic surfaces in aqueous solution is considered as hydrophobic interaction. Because both the spike protein and hydrophobic surfaces carry the overall negative charges, the overall electrostatic interaction between spike protein and hydrophobic surfaces in aqueous solution is repulsive. However, spike protein could display positively charged sites and negatively charged sites. The contribution of electrostatic attraction between the positively charged sites of spike protein and polymer surfaces could not be ruled out. For the metals, the adhesion energy with spike protein lies in a wide range from 2 to 9 mJ/m<sup>2</sup>, which relies on the binding capability of metals with spike protein. In the metallic materials investigated, copper exhibits the strongest adhesion with spike protein followed by SS, gold, and alumina foil.

It is worth mentioning that the oriented spike protein could be a perfect molecular model for the experimental design; meanwhile, the surrounding temperature, pH, saline concentration, and/or shrinkage because of dehydration could all affect the virion shape and size, as well as the orientation of spike protein on surfaces. In this work, despite the random orientation of the S1 subunits on AFM tips (the exposed subunits of spike protein), over 600 force measurement events have been collected for each S1-surface pair, and the statistical plots can reflect the trend of virion adhesion on various surfaces. It is noted that the real contact region for the force measurements between an AFM tip (a radius of 25–35 nm) and a substrate surface is only at the nanoscopic level, and thus, the influence of surface roughness on the adhesion energy has been dramatically reduced. The uniform distribution of adhesion forces, which can also be reflected from the histogram of adhesion forces (Figures S3–S5), ensures the accuracy of force measurements. It is also noted that the rough alumina foil and copper foil lie in a similar regime of adhesion energy with smooth SS and gold coating (metals), while the rough nitrile glove, safety glass, medical mask (polypropylene), and polyethylene plastic lie in a similar region with smooth PS and PTFE surfaces (hydrophobic polymers).

It is known that the interfacial adhesion of solid materials can be mediated by tuning their surface properties.<sup>47–51</sup> Because the surface hydrophilicity of materials plays an important role in their interactions with the spike protein, it is reasonable to conclude that glass-based materials (e.g., windows, mirrors, glass doors, and glass screens) exhibit relatively low stickiness for the new coronavirus compared to the plastics and fabrics. Nevertheless, the stickiness of the new coronavirus on glass can become strong once the glass is contaminated by organics. It is worth noting that the commonly used personal protective equipment (PPE), including medical masks (polypropylene), safety glass, and nitrile gloves, also displays very high adhesion energy (6–11 mJ/m<sup>2</sup>), which could be altered by applying the superhydrophilic or superhydrophobic coatings. In addition, the addition of alcohol (e.g., methanol, ethanol, and isopropyl alcohol) into aqueous media is known to suppress the hydrophobic interaction,<sup>52–54</sup> and thus, the new coronavirus stuck on plastic, fabric, and PPE could be washed off by the alcohol even if the alcohol is insufficiently concentrated to kill the virus. Similarly, the surfactant-containing aqueous solution is also an efficient approach to eliminate the hydrophobic interaction and remove the new coronavirus.

The adhesion of spike protein with solid materials could be an important contributor to the substance-dependent persistence of SARS-CoV-2 virions. There were few reports on the persistence of SARS-CoV-2 on typical substrates under a water-based environment,<sup>9,10</sup> which limit the data availability at this time. The persistence of SARS-CoV-2 was reported to be 4 h for copper, 2 days for SS, and 3 days for plastic.<sup>9</sup> Based on our studies, the adhesion energy of spike protein interacting with copper, SS, and plastic is 8.93, 7.48, and 7.64 mJ/m<sup>2</sup>, respectively. It has been reported that the adhesion could lead to the compression of virus, which disrupts the 3D structure of proteins and ultimately inactivates the virus.<sup>55,56</sup> Thus, the higher adhesion for copper could be one contributor to the shorter persistence of coronavirus on copper. Although the adhesion for SS and plastic is similar, other factors such as the complex metal antiviral mechanism could play a critical role in the persistence of coronavirus.



### 3. CONCLUSIONS

In this work, we systematically quantified the intermolecular interactions between spike protein (the corona-like component of the SARS-CoV-2 virion) and a series of inanimate surfaces (e.g., glass, plastics, metals, and fabrics) under a simulated respiratory droplet environment at the nanoscale. The environmental factors, including pH and temperature, were observed to affect the spike protein binding. According to the quantitative AFM force measurements, the adhesion of spike protein was (i) very weak on hydrophilic inorganics (e.g., glass) because of the lack of substantial hydrogen bonding formation, (ii) relatively high on metal surfaces because of the strong coordination interaction, and (iii) very strong on hydrophobic polymers (e.g., PS, PTFE, plastics, and PPE), attributed to the hydrophobic interaction. The alternation of surface hydrophilicity of materials or addition of chemical additives could effectively modulate the hydrophobic interaction and even tune the interaction mechanism between hydrogen bonding and hydrophobic interaction, which would be a promising strategy to mediate the adhesion of spike protein and stickiness of new coronavirus. Additionally, the adhesion of spike protein with solid materials could be an important contributor to the substance-dependent persistence of SARS-CoV-2 virions. The developed protein–surface model database for SARS-CoV-2 with respect to their intermolecular and surface interactions will provide scientific guidance for developing effective preventive strategies to prohibit virus transmission via surface contaminations.

### 4. EXPERIMENTAL METHODS

**4.1. Materials.** Sodium chloride (NaCl, ACS reagent grade), hydrochloric acid (HCl, ACS reagent grade), and sodium hydroxide (NaOH, ACS reagent grade) were purchased from Fisher Scientific. 11-Mercaptoundecanoic acid ( $\text{HS}(\text{CH}_2)_{10}\text{COOH}$ , 98%), N-hydroxysuccinimide (NHS,  $\text{C}_4\text{H}_5\text{NO}_3$ , and 98%), N-(3-Dimethylamino-propyl)-N'-ethylcarbodiimide hydrochloride (EDC,  $\text{C}_8\text{H}_{17}\text{N}_3\cdot\text{HCl}$ , 98%), and phosphate buffered saline (pH 7.4) were purchased from MilliporeSigma. COVID-19 spike S1 coronavirus active protein (purity >90% by sodium dodecyl sulfate polyacrylamide gel electrophoresis and molecular weight of 120 kDa) was purchased from MyBioSource, Inc. All the chemicals were used as received without further purification, and all aqueous solutions were prepared using Milli-Q water (Millipore deionized,  $18.2\text{ M}\Omega\cdot\text{cm}$  resistivity).

**4.2. Preparation of the Spike Protein-Functionalized AFM Probe and Solid Substrates.** Spike protein solution was prepared by dissolving 0.1 mg COVID-19 spike S1 coronavirus active protein in 2 mL PbS buffer (pH 7.4), and the prepared spike protein solution was stored at  $-20\text{ }^\circ\text{C}$ . The gold-coated AFM probes were cleaned by UV/ozone treatment for 30 min and then immersed in 10 mM 11-mercaptoundecanoic acid in ethanol overnight. After the self-assembly via the Au–S bonding, the COOH-functionalized AFM probes were washed with ethanol to remove the physisorbed thiol, dried with high-purity nitrogen, and then immersed in an aqueous solution containing 20 mM NHS and 40 mM EDC to activate the COOH functional groups on AFM probes. After 1 h, the NHS/EDC-activated AFM probes were immersed in 0.05 mg/mL spike protein in PbS buffer for 2 h to prepare the protein-functionalized AFM probes. Thereafter, the protein-functionalized AFM probes were washed with Milli-Q water, dried with high-purity nitrogen, and immediately used for characterization and force measurements.

A glass sheet and a silicon wafer (with an oxidation layer) were washed with ethanol and water three times, dried with high-purity nitrogen, and then cleaned by UV/ozone treatment for 10 min. Gold-coated silicon wafers were cleaned with a typical RCA procedure with slight modifications.<sup>57,58</sup> The gold wafer shards were first sonicated in methanol for 5 min, dried with high-purity nitrogen, and immersed in

RCA1 solution (Milli-Q water:30%  $\text{NH}_4\text{OH}$ :30%  $\text{H}_2\text{O}_2 = 6:1:1$  volume ratio) and RCA2 solution (Milli-Q water:37.5%  $\text{HCl}$ :30%  $\text{H}_2\text{O}_2 = 6:1:1$  volume ratio) for 5 min at  $80\text{ }^\circ\text{C}$ . The gold wafer shards were dried and went through argon plasma to further remove residues. Alumina and copper were obtained directly from the aluminum foil and copper foil, which were cleaned with ethanol and water three times. A QSX 304 SS sensor (SS2343, Biolin Scientific) was cleaned by immersing the sensor in 1% Hellmanex II for 30 min, rinsed with Milli-Q water, and dried with high-purity nitrogen. The PS surface was prepared by spin coating PS solution (0.5 wt % in toluene) on silicon wafer at 2000 rpm, and the spin-coated surface was dried under vacuum overnight to completely remove the residual solvent. The plastic bottle of Nestlé pure life natural spring water and a Uline medical mask, which are ubiquitous in daily life and have drawn much attention, were selected as the representative samples of the polyethylene surface and polypropylene surface, respectively. PTFE, polyethylene plastic, medical mask (polypropylene), safety glass, and nitrile glove were cleaned with ethanol and water three times. All the samples were immediately used for the force measurements after the cleaning procedure.

**4.3. Characterization.** Several selected solid surfaces before and after spike protein adsorption were characterized by AFM topography imaging. The COOH-functionalized and protein-functionalized AFM probes were subjected to AFM imaging, contact angle measurements, HIM, and AES. The imaging of the solid surfaces and the cantilever base of AFM probes was performed using the tapping mode of a Dimension Icon AFM (Bruker, Santa Barbara, CA, USA). Typically, the functionalized gold-coated AFM probe was glued onto the AFM scanning stage by double-sided tape, and then a silicon AFM probe was used to perform the imaging on the cantilever base of the AFM probe. The water contact angle on the cantilever base of AFM probes was measured using the sessile drop method with a contact angle goniometer (ramé-hart instrument Co., NJ, USA). The average water contact angle was reported based on the measurements of few microliter water droplets on at least three independently prepared AFM probes. It is noted that AFM imaging and contact angle measurements were difficult to conduct directly on the AFM cantilever and AFM tip because of their small size, and thus, these two tests were conducted on the AFM cantilever base of the AFM probe with the same material composition as the AFM cantilever and tip. HIM of AFM tips was conducted using a Zeiss Orion NanoFab (Carl Zeiss AG, Oberkochen, Germany) equipped with the He beam, while AES of AFM tips was performed using a JAMP-9500F Field Emission Auger Microprobe (JEOL, MA, USA) equipped with a Shottky field emitter, which produces an electron probe diameter of 3–8 nm.

**4.4. Helium Ion Microscopy.** HIM was performed using the Zeiss Orion NanoFab (Zeiss Peabody, MA, USA) tool at ProVIS–Centre for Chemical Microscopy at the Helmholtz–Centre for Environmental Research, Leipzig, Germany. For imaging, the landing energy of the ions was set to 25 keV, and a  $10\text{ }\mu\text{m}$  aperture was used. By variation of the spot-control parameter (values between 4 and 6), the ion-beam current was adjusted to about 1.0 pA measured at the blanker of the tool. For image acquisition, secondary electrons were detected using an Everhard–Thornley detector. Typically dwell time and line-averaging were set to  $0.2\text{ }\mu\text{s}$  and 64, respectively. All micrographs were acquired at a pixel resolution of  $2048 \times 2048$ . To achieve a more 3D impression of the images, the stage was tilted by  $45^\circ$ . During imaging, the flood-gun was switched on and used in line-flooding mode such that charging effects could be avoided. Prior to imaging, the resolution of the tool was checked to be better than 3 nm using edge contrast on an empty sample holder.

**4.5. AFM Force Measurements.** The interaction forces between the protein-functionalized AFM tips and a variety of solid materials were measured under simulated respiratory droplet conditions using an MFP-3D AFM (Asylum Research, Santa Barbara, CA, USA). Typically, the AFM tip was positioned over solid substrates, following which the AFM tip was driven at a loading rate of  $0.1\text{ }\mu\text{N/s}$  to approach the substrates until a maximum force load of 5 nN was achieved. After 1 s contact, the AFM tip was retracted from the

substrates at a loading rate of 0.1  $\mu\text{N/s}$ . The approach–retraction force measurements were conducted for 300–500 cycles on several different samples for the same material and several different locations for the same sample, based on which the distribution of adhesion forces was reported.

## ■ ASSOCIATED CONTENT

### SI Supporting Information

The Supporting Information is available free of charge at <https://pubs.acs.org/doi/10.1021/acsami.0c16800>.

AFM topography images ( $2 \times 2 \mu\text{m}^2$ ), high-resolution HIM, histogram of normalized adhesion force, and zeta potential of spike protein subunit S1 (PDF)

## ■ AUTHOR INFORMATION

### Corresponding Authors

**Jifang Liu** – Sixth Affiliated Hospital of Guangzhou Medical University, Qingyuan People's Hospital, Guangzhou Medical University, Guangdong 511500, China;  
Email: [yzhbb2012@126.com](mailto:yzhbb2012@126.com)

**Hongbo Zeng** – Department of Chemical and Materials Engineering, University of Alberta, Edmonton, Alberta T6G 1H9, Canada; [orcid.org/0000-0002-1432-5979](https://orcid.org/0000-0002-1432-5979);  
Phone: +1-780-492-1044; Email: [hongbo.zeng@ualberta.ca](mailto:hongbo.zeng@ualberta.ca); Fax: +1-780-492-2881

### Authors

**Lei Xie** – School of Minerals Processing and Bioengineering, Central South University, Changsha 410083, China;  
Department of Chemical and Materials Engineering, University of Alberta, Edmonton, Alberta T6G 1H9, Canada; [orcid.org/0000-0003-3520-4815](https://orcid.org/0000-0003-3520-4815)

**Fenglin Liu** – Institute of Biomedical and Health Engineering, Shenzhen Institutes of Advanced Technology, Chinese Academy of Sciences, Shenzhen 518035, China;  
[orcid.org/0000-0002-6995-0552](https://orcid.org/0000-0002-6995-0552)

Complete contact information is available at:  
<https://pubs.acs.org/doi/10.1021/acsami.0c16800>

### Author Contributions

<sup>†</sup>L.X. and F.L. contributed equally to this work.

### Notes

The authors declare no competing financial interest.

## ■ ACKNOWLEDGMENTS

We gratefully acknowledge the financial support from the Natural Sciences and Engineering Research Council of Canada (NSERC), the Canada Foundation for Innovation (CFI), the Alberta Advanced Education & Technology Small Equipment Grants Program (AET/SEGP), the Canada Research Chairs Program (H.Z.), and the NSERC postdoctoral fellowship (F.L.).

## ■ REFERENCES

- (1) Peng, X.; Xu, X.; Li, Y.; Cheng, L.; Zhou, X.; Ren, B. Transmission Routes of 2019-Ncov and Controls in Dental Practice. *Int. J. Oral Sci.* **2020**, *12*, 9.
- (2) Li, R.; Pei, S.; Chen, B.; Song, Y.; Zhang, T.; Yang, W.; Shaman, J. Substantial Undocumented Infection Facilitates the Rapid Dissemination of Novel Coronavirus (Sars-Cov-2). *Science* **2020**, *368*, 489–493.
- (3) Sohrabi, C.; Alsafi, Z.; O'Neill, N.; Khan, M.; Kerwan, A.; Al-Jabir, A.; Iosifidis, C.; Agha, R. World Health Organization Declares

Global Emergency: A Review of the 2019 Novel Coronavirus (Covid-19). *Int. J. Surg.* **2020**, *76*, 71–76.

(4) Chinazzi, M.; Davis, J. T.; Ajelli, M.; Gioannini, C.; Litvinova, M.; Merler, S.; Piontti, A. P.; Mu, K.; Rossi, L.; Sun, K. The Effect of Travel Restrictions on the Spread of the 2019 Novel Coronavirus (Covid-19) Outbreak. *Science* **2020**, *368*, 395–400.

(5) Kissler, S. M.; Tedijanto, C.; Goldstein, E.; Grad, Y. H.; Lipsitch, M. Projecting the Transmission Dynamics of Sars-Cov-2 through the Postpandemic Period. *Science* **2020**, *368*, 860–868.

(6) Lai, C. C.; Shih, T. P.; Ko, W. C.; Tang, H. J.; Hsueh, P. R. Severe Acute Respiratory Syndrome Coronavirus 2 (Sars-Cov-2) and Coronavirus Disease-2019 (Covid-19): The Epidemic and the Challenges. *Int. J. Antimicrob. Agents* **2020**, *55*, 105924.

(7) Wang, W.; Xu, Y.; Gao, R.; Lu, R.; Han, K.; Wu, G.; Tan, W. Detection of Sars-Cov-2 in Different Types of Clinical Specimens. *JAMA* **2020**, *323*, 1843–1844.

(8) Guan, W.; Ni, Z.; Hu, Y.; Liang, W.; Ou, C.; He, J.; Liu, L.; Shan, H.; Lei, C.; Hui, D. Clinical Characteristics of Coronavirus Disease 2019 in China. *N. Engl. J. Med.* **2020**, *382*, 1708–1720.

(9) Van Doremalen, N.; Bushmaker, T.; Morris, D. H.; Holbrook, M. G.; Gamble, A.; Williamson, B. N.; Tamin, A.; Harcourt, J. L.; Thornburg, N. J.; Gerber, S. I. Aerosol and Surface Stability of Sars-Cov-2 as Compared with Sars-Cov-1. *N. Engl. J. Med.* **2020**, *382*, 1564–1567.

(10) Duan, S.; Zhao, X.; Wen, R.; Huang, J.; Pi, G.; Zhang, S.; Han, J.; Bi, S.; Ruan, L.; Dong, X. Stability of Sars Coronavirus in Human Specimens and Environment and Its Sensitivity to Heating and Uv Irradiation. *Biomed. Environ. Sci.* **2003**, *16*, 246–255.

(11) Kampf, G.; Todt, D.; Pfaender, S.; Steinmann, E. Persistence of Coronaviruses on Inanimate Surfaces and Their Inactivation with Biocidal Agents. *J. Hosp. Infect.* **2020**, *104*, 246–251.

(12) van Doremalen, N.; Bushmaker, T.; Munster, V. J. Stability of Middle East Respiratory Syndrome Coronavirus (Mers-Cov) under Different Environmental Conditions. *Eur. Commun. Dis. Bull.* **2013**, *18*, 20590.

(13) Fischer, R.; Judson, S.; Miazgowiec, K.; Bushmaker, T.; Prescott, J.; Munster, V. J. Ebola Virus Stability on Surfaces and in Fluids in Simulated Outbreak Environments. *Emerg. Infect. Dis.* **2015**, *21*, 1243–1246.

(14) Wrapp, D.; Wang, N. S.; Corbett, K. S.; Goldsmith, J. A.; Hsieh, C. L.; Abiona, O.; Graham, B. S.; McLellan, J. S. Cryo-Em Structure of the 2019-Ncov Spike in the Prefusion Conformation. *Science* **2020**, *367*, 1260–1263.

(15) Walls, A. C.; Park, Y. J.; Tortorici, M. A.; Wall, A.; McGuire, A. T.; Veerler, D. Structure, Function, and Antigenicity of the Sars-Cov-2 Spike Glycoprotein. *Cell* **2020**, *181*, 281–292.e6.

(16) Zhang, L.; Lin, D.; Sun, X.; Curth, U.; Drosten, C.; Sauerherring, L.; Becker, S.; Rox, K.; Hilgenfeld, R. Crystal Structure of Sars-Cov-2 Main Protease Provides a Basis for Design of Improved Alpha-Ketoamide Inhibitors. *Science* **2020**, *368*, 409–412.

(17) Yan, R.; Zhang, Y.; Li, Y.; Xia, L.; Guo, Y.; Zhou, Q. Structural Basis for the Recognition of Sars-Cov-2 by Full-Length Human Ace2. *Science* **2020**, *367*, 1444–1448.

(18) Gui, M.; Song, W.; Zhou, H.; Xu, J.; Chen, S.; Xiang, Y.; Wang, X. Cryo-Electron Microscopy Structures of the Sars-Cov Spike Glycoprotein Reveal a Prerequisite Conformational State for Receptor Binding. *Cell Res.* **2017**, *27*, 119–129.

(19) Shang, J.; Ye, G.; Shi, K.; Wan, Y.; Luo, C.; Aihara, H.; Geng, Q.; Auerbach, A.; Li, F. Structural Basis of Receptor Recognition by Sars-Cov-2. *Nature* **2020**, *581*, 221–224.

(20) Yuan, M.; Wu, N. C.; Zhu, X. Y.; Lee, C. C. D.; So, R. T. Y.; Lv, H. B.; Mok, C. K. P.; Wilson, I. A. A Highly Conserved Cryptic Epitope in the Receptor Binding Domains of Sars-Cov-2 and Sars-Cov. *Science* **2020**, *368*, 630–633.

(21) Hinterdorfer, P.; Dufrêne, Y. F. Detection and Localization of Single Molecular Recognition Events Using Atomic Force Microscopy. *Nat. Methods* **2006**, *3*, 347–355.

(22) Xie, L.; Gong, L.; Zhang, J.; Han, L.; Xiang, L.; Chen, J.; Liu, J.; Yan, B.; Zeng, H. A Wet Adhesion Strategy Via Synergistic Cation- $\Pi$



and Hydrogen Bonding Interactions of Antifouling Zwitterions and Mussel-Inspired Binding Moieties. *J. Mater. Chem. A* **2019**, *7*, 21944–21952.

(23) Yu, J.; Jackson, N. E.; Xu, X.; Brettmann, B. K.; Ruths, M.; de Pablo, J. J.; Tirrell, M. Multivalent Ions Induce Lateral Structural Inhomogeneities in Polyelectrolyte Brushes. *Sci. Adv.* **2017**, *3*, No. eaao1497.

(24) Yu, J.; Jackson, N. E.; Xu, X.; Morgenstern, Y.; Kaufman, Y.; Ruths, M.; De Pablo, J. J.; Tirrell, M. Multivalent Counterions Diminish the Lubricity of Polyelectrolyte Brushes. *Science* **2018**, *360*, 1434–1438.

(25) Tian, Y.; Pesika, N.; Zeng, H.; Rosenberg, K.; Zhao, B.; McGuiggan, P.; Autumn, K.; Israelachvili, J. Adhesion and Friction in Gecko Toe Attachment and Detachment. *Proc. Natl. Acad. Sci. U. S. A.* **2006**, *103*, 19320–19325.

(26) Zhao, Y.; Wu, Y.; Wang, L.; Zhang, M.; Chen, X.; Liu, M.; Fan, J.; Liu, J.; Zhou, F.; Wang, Z. Bio-Inspired Reversible Underwater Adhesive. *Nat. Commun.* **2017**, *8*, 1–8.

(27) Zhang, J.; Xiang, L.; Yan, B.; Zeng, H. Nanomechanics of Anion- $\Pi$  Interaction in Aqueous Solution. *J. Am. Chem. Soc.* **2020**, *142*, 1710–1714.

(28) Yoo, H. Y.; Iordachescu, M.; Huang, J.; Hennebert, E.; Kim, S.; Rho, S.; Foo, M.; Flammang, P.; Zeng, H.; Hwang, D. Sugary Interfaces Mitigate Contact Damage Where Stiff Meets Soft. *Nat. Commun.* **2016**, *7*, 1–8.

(29) Kim, S.; Huang, J.; Lee, Y.; Dutta, S.; Yoo, H. Y.; Jung, Y. M.; Jho, Y.; Zeng, H.; Hwang, D. S. Complexation and Coacervation of Like-Charged Polyelectrolytes Inspired by Mussels. *Proc. Natl. Acad. Sci. U. S. A.* **2016**, *113*, E847–E853.

(30) Lim, C.; Huang, J.; Kim, S.; Lee, H.; Zeng, H.; Hwang, D. S. Nanomechanics of Poly (Catecholamine) Coatings in Aqueous Solutions. *Angew. Chem., Int. Ed.* **2016**, *55*, 3342–3346.

(31) Zhang, C.; Gong, L.; Xiang, L.; Du, Y.; Hu, W.; Zeng, H.; Xu, Z.-K. Deposition and Adhesion of Polydopamine on the Surfaces of Varying Wettability. *ACS Appl. Mater. Interfaces* **2017**, *9*, 30943–30950.

(32) Butt, H.-J.; Cappella, B.; Kappl, M. Force Measurements with the Atomic Force Microscope: Technique, Interpretation and Applications. *Surf. Sci. Rep.* **2005**, *59*, 1–152.

(33) Mi, X.; Bromley, E. K.; Joshi, P. U.; Long, F.; Heldt, C. L. Virus Isoelectric Point Determination Using Single-Particle Chemical Force Microscopy. *Langmuir* **2019**, *36*, 370–378.

(34) Said, N.; Chatzinotas, A.; Schmidt, M. Have an Ion on It: The Life-Cycle of *Bdellovibrio Bacteriovorus* Viewed by Helium-Ion Microscopy. *Adv. Biosys.* **2019**, *3*, 1800250.

(35) Gu, Y.; Li, D. The Z-Potential of Glass Surface in Contact with Aqueous Solutions. *J. Colloid Interface Sci.* **2000**, *226*, 328–339.

(36) Israelachvili, J. N. *Intermolecular and Surface Forces*; Academic press, 2015.

(37) Yamashita, M. M.; Wesson, L.; Eisenman, G.; Eisenberg, D. Where Metal Ions Bind in Proteins. *Proc. Natl. Acad. Sci. U. S. A.* **1990**, *87*, 5648–5652.

(38) Xie, L.; Wang, J.; Shi, C.; Huang, J.; Zhang, H.; Liu, Q.; Liu, Q.; Zeng, H. Probing Surface Interactions of Electrochemically Active Galena Mineral Surface Using Atomic Force Microscopy. *J. Phys. Chem. C* **2016**, *120*, 22433–22442.

(39) Xie, L.; Wang, J.; Shi, C.; Cui, X.; Huang, J.; Zhang, H.; Liu, Q.; Liu, Q.; Zeng, H. Mapping the Nanoscale Heterogeneity of Surface Hydrophobicity on the Sphalerite Mineral. *J. Phys. Chem. C* **2017**, *121*, 5620–5628.

(40) Xie, L.; Lu, Q.; Mao, X.; Wang, J.; Han, L.; Hu, J.; Lu, Q.; Wang, Y.; Zeng, H. Probing the Intermolecular Interaction Mechanisms between Humic Acid and Different Substrates with Implications for Its Adsorption and Removal in Water Treatment. *Water Res.* **2020**, *176*, 115766.

(41) Sheu, S.-Y.; Yang, D.-Y.; Selzle, H.; Schlag, E. Energetics of Hydrogen Bonds in Peptides. *Proc. Natl. Acad. Sci. U. S. A.* **2003**, *100*, 12683–12687.

(42) Lu, Q.; Oh, D. X.; Lee, Y.; Jho, Y.; Hwang, D. S.; Zeng, H. Nanomechanics of Cation- $\Pi$  Interactions in Aqueous Solution. *Angew. Chem., Int. Ed.* **2013**, *52*, 3944–3948.

(43) Donaldson, S. H., Jr.; Røyne, A.; Kristiansen, K.; Rapp, M. V.; Das, S.; Gebbie, M. A.; Lee, D. W.; Stock, P.; Valtiner, M.; Israelachvili, J. Developing a General Interaction Potential for Hydrophobic and Hydrophilic Interactions. *Langmuir* **2014**, *31*, 2051–2064.

(44) Huang, C.-J.; Wang, L.-C.; Liu, C.-Y.; Chiang, A. S.; Chang, Y.-C. Natural Zwitterionic Organosulfurs as Surface Ligands for Antifouling and Responsive Properties. *Biointerphases* **2014**, *9*, No. 029010.

(45) Cui, X.; Shi, C.; Xie, L.; Liu, J.; Zeng, H. Probing Interactions between Air Bubble and Hydrophobic Polymer Surface: Impact of Solution Salinity and Interfacial Nanobubbles. *Langmuir* **2016**, *32*, 11236–11244.

(46) Stock, P.; Utzig, T.; Valtiner, M. Direct and Quantitative Afn Measurements of the Concentration and Temperature Dependence of the Hydrophobic Force Law at Nanoscopic Contacts. *J. Colloid Interface Sci.* **2015**, *446*, 244–251.

(47) Cho, Y.; Kim, G.; Cho, Y.; Lee, S. Y.; Minsky, H.; Turner, K. T.; Gianola, D. S.; Yang, S. Orthogonal Control of Stability and Tunable Dry Adhesion by Tailoring the Shape of Tapered Nanopillar Arrays. *Adv. Mater.* **2015**, *27*, 7788–7793.

(48) Stuart, M. A. C.; Huck, W. T.; Genzer, J.; Müller, M.; Ober, C.; Stamm, M.; Sukhorukov, G. B.; Szleifer, I.; Tsukruk, V. V.; Urban, M. Emerging Applications of Stimuli-Responsive Polymer Materials. *Nat. Mater.* **2010**, *9*, 101–113.

(49) Liu, M.; Wang, S.; Jiang, L. Nature-Inspired Superwettability Systems. *Nat. Rev. Mater.* **2017**, *2*, 1–17.

(50) Brown, P.; Bushmelev, A.; Butts, C. P.; Cheng, J.; Eastoe, J.; Grillo, I.; Heenan, R. K.; Schmidt, A. M. Magnetic Control over Liquid Surface Properties with Responsive Surfactants. *Angew. Chem., Int. Ed.* **2012**, *51*, 2414–2416.

(51) Gong, M. M.; Sinton, D. Turning the Page: Advancing Paper-Based Microfluidics for Broad Diagnostic Application. *Chem. Rev.* **2017**, *117*, 8447–8480.

(52) Ma, C. D.; Wang, C.; Acevedo-Vélez, C.; Gellman, S. H.; Abbott, N. L. Modulation of Hydrophobic Interactions by Proximally Immobilized Ions. *Nature* **2015**, *517*, 347.

(53) Xie, L.; Cui, X.; Gong, L.; Chen, J.; Zeng, H. Recent Advances in the Quantification and Modulation of Hydrophobic Interactions for Interfacial Applications. *Langmuir* **2020**, *36*, 2985–3003.

(54) Xie, L.; Yang, D.; Lu, Q.; Zhang, H.; Zeng, H. Role of Molecular Architecture in the Modulation of Hydrophobic Interactions. *Curr. Opin. Colloid Interface Sci.* **2019**, *47*, 58–69.

(55) Thurman, R. B.; Gerba, C. P.; Bitton, G. The Molecular Mechanisms of Copper and Silver Ion Disinfection of Bacteria and Viruses. *Crit. Rev. Environ. Sci. Technol.* **1989**, *18*, 295–315.

(56) Scully, J. R. The Covid-19 Pandemic, Part 1: Can Antimicrobial Copper-Based Alloys Help Suppress Infectious Transmission of Viruses Originating from Human Contact with High-Touch Surfaces? *Corrosion* **2020**, *76*, S23–S27.

(57) Liu, F.; Lubber, E. J.; Huck, L. A.; Olsen, B. C.; Buriak, J. M. Nanoscale Plasmonic Stamp Lithography on Silicon. *ACS Nano* **2015**, *9*, 2184–2193.

(58) Liu, F.; Hauger, T. C.; Olsen, B. C.; Lubber, E. J.; Buriak, J. M. Polymers, Plasmons, and Patterns: Mechanism of Plasmon-Induced Hydrosilylation on Silicon. *Chem. Mater.* **2016**, *28*, 9158–9168.